Journal of The Electrochemical Society, **154** (1) B106-B116 (2007)
0013-4651/2006/154(1)/B106/11/$20.00 © The Electrochemical Society

Transport Phenomena in Elevated Temperature PEM Fuel Cells

Puneet K. Sinha,[a,*] Chao-Yang Wang,[a,,z] and Uwe Beuscher[b]**

[a]*Department of Mechanical and Nuclear Engineering and Electrochemical Engine Center, The Pennsylvania State University, University Park, Pennsylvania 16802, USA*
[b]*Gore Fuel Cell Technologies, W.L. Gore & Associates, Incorporated, Elkton, Maryland 21921, USA*

There is a recognized need for operation of polymer electrolyte membrane (PEM) fuel cells at higher than 80°C for automotive applications. Electrochemically, higher temperature results in better kinetics of oxygen oxidation reaction but more difficult membrane hydration. These consequences call for a detailed study of electrochemical and transport phenomena at such operating temperatures. In this work, a three-dimensional, nonisothermal model was used to investigate the performance of PEM fuel cells operating at 95°C under various operating conditions. The numerical model is first validated against experimental data for a 25 cm^2 cell, after which a detailed analysis of species, heat, and charge transport is presented based on a single-channel unit cell. A brief study of the effect of flow-field design on cell performance is also presented. Numerical studies reveal that at 95°C operation, oxygen transport and its depletion along the flow direction play a critical role in cell performance, even under low humidity conditions.
 [DOI: 10.1149/1.2393014]

Manuscript submitted March 24, 2006; revised manuscript received August 31, 2006. Available electronically December 1, 2006.

Development of proton exchange membrane (PEM) fuel cell technology for vehicular application requires higher than 80°C operating temperature to enhance heat dissipation capability of a fuel cell stack, as well as its tolerance to minute amounts of carbon monoxide present in the fuel stream. Rogg et al.[1] recognized that cooling is a key problem for fuel cell engines in spite of their high efficiency for vehicles. This cooling duty cannot be met by using large radiators because of space limitations in a vehicle. High fuel cell temperature facilitates heat rejection, resulting in a smaller radiator size. Mallant[2] investigated the effect of pressure and temperature on the heating and cooling load of a PEM fuel cell system. His study emphasized the need for high-temperature operation for better water and thermal management of the system. Various studies[3,4] show significant improvement in CO tolerance at 100–115°C, as the kinetics of desorption of CO is rapid at high temperatures, thus providing more free catalytic sites to hydrogen molecules.

Although the need for high-temperature operation has been highlighted, operation above 80°C is constrained by membrane dryout, thermal degradation, and low ionic conductivity. In recent years, there has been significant progress in the development of membrane materials, allowing for operation at higher temperatures while preserving good proton conductivity. Malhotra et al.[5] proposed the use of Nafion membranes soaked in phosphotungstic acid (PTA) solution for operations at temperatures above 100°C. Yang et al.[6] studied the performance of fuel cells with various composite and nonaqueous membranes operating at or above 100°C. Their study showed that in fuel cells with composite membranes, at elevated temperatures, performance is improved by allowing operation at low relative humidity. Ramani et al.[7,8] investigated Nafion/HPA (hetropolyacid) composite membranes for high temperatures up to 120°C and at low inlet humidity, an environment well suited for automotive applications. Their study demonstrated the ability of such membranes to perform satisfactorily in high-temperature, low-humidity environments. Studies carried out by Adjemian et al.[9] exhibited lower resistances and higher current densities for silicon oxide Nafion membranes at 130 and 140°C as compared to unmodified Nafion membranes. Mathias et al.[10] presented an excellent review of membrane, electrocatalyst, and catalyst-support durability of high-temperature membrane electrode assemblies (MEAs) for automotive applications.

The saturation pressure of water is a strong function of temperature. Increase in the temperature from 80 to 95°C doubles the saturation pressure, which in turn increases the saturation concentration of water and makes membrane hydration difficult at 95°C operating temperature. However, an increase in the operating temperature also results in better ORR kinetics. These consequences of high-temperature operation necessitate a close examination of transport phenomena for fuel cell operation above 80°C. Several experimental investigations of PEM fuel cell performance at temperatures above 80°C[6-9] are available in the literature, but none of these address these consequences of fuel cell operation above 80°C.

In this paper, we present a model to describe electrochemical and transport phenomena for a PEM cell operating at elevated temperatures. The model is first validated against experimental data, after which electrochemical and transport phenomena in a PEM fuel cell operating at 95°C are explored in detail using a single-channel cell. Finally, a comparison of fuel cell operated at 95°C with parallel flow-field design and serpentine flow-field design is presented.

Physical and Numerical Model

The present three-dimensional, nonisothermal, electrochemical, and transport fully coupled PEM fuel cell model has been developed based on the previous work of Um et al.,[11] Meng and Wang,[12] and Ju et al.[13] The complete set of conservation equations of mass, momentum, species, energy, and charge (both protons and electrons) are solved, with proper account of electrochemical kinetics. The thermal model considers all 11 subregions of a PEM fuel cell—gas channels, macro and micro gas diffusion layers, catalyst layers, bipolar plates on both anode and cathode side, and the ionomeric membrane. The following assumptions are made in the present model:

1. Ideal gas mixtures.
2. Isotropic and homogenous electrode, catalyst layers and membrane.
3. Incompressible and laminar flow due to small pressure gradient and flow velocities.
4. Single-phase assumption for water transport.

Table I presents conservation equations of mass, momentum, chemical species, proton, electron, and energy.

Description of governing equations.— Mass and momentum equations are solved to obtain the flow field. The source terms in momentum equations are added based on Darcy's law, representing an extra drag force proportional to the fluid viscosity and velocity, and inversely proportional to the permeability of porous media. Superficial velocities are used in continuity and momentum conservation equations to automatically ensure mass flux continuity at the

* Electrochemical Society Student Member.
** Electrochemical Society Active Member.
z E-mail address: cxw31@psu.edu

Table I. Single phase nonisothermal PEMFC model; governing equations and source terms.

	Conservation equations	Source terms
Mass	$\nabla \cdot (\rho \mathbf{u}) = 0$	
Momentum	$\frac{1}{\varepsilon^2} \nabla \cdot (\rho \mathbf{u}\mathbf{u}) = -\nabla p + \nabla \cdot \tau + S_u$	In diffusion and catalyst layers: $S_u = -\frac{\mu}{K}\mathbf{u}$
Species	$\nabla \cdot (\mathbf{u}C_k) = \nabla \cdot (D_k^{eff} \nabla C_k) + S_k$	In catalyst layers: $S_k = -\frac{s_k j}{nF}$ For water in catalyst layers: $S_k = -\nabla \cdot \left(\frac{n_d}{F} I\right) - \frac{s_k j}{nF}$
Proton	$\nabla \cdot (\kappa^{eff} \nabla \Phi_e) + S_\Phi = 0$	In catalyst layers: $S_\Phi = j$
Electron	$\nabla \cdot (\sigma_s^{eff} \nabla \phi_s) + S_\Phi = 0$	In catalyst layers: $S_\Phi = -j$
Energy	$\nabla \cdot (\rho c_p \mathbf{u}T) = \nabla \cdot (k^{eff} \nabla T) + S_T$	In catalyst layers: $S_T = j\left(\eta + T\frac{dU_o}{dT}\right) + \frac{I^2}{\kappa^{eff}}$ In membrane: $S_T = \frac{I^2}{\kappa^{eff}}$

Electrochemical reaction:

$$\Sigma_k s_k M_k^z = ne^- \quad \text{where} \begin{cases} M_k \equiv \text{chemical formula of species k} \\ s_k \equiv \text{stoichiometry coefficient} \\ n \equiv \text{number of electrons transferred} \end{cases}$$

Hydrogen oxidation reaction (HOR) in anode side: $H_2 - 2H^+ = 2e^-$
Oxygen reduction reaction (ORR) in cathode side: $2H_2O - O_2 - 4H^+ = 4e^-$

interface between porous GDL and nonporous gas channels. The intrinsic transport properties in the porous media are modified into effective transport properties to account for the porosity and tortuosity of the porous media. Species concentration equations are solved to obtain hydrogen, oxygen, and water distribution, with implementation of source terms based on electrochemical kinetics. The proton conservation equation is solved inside the MEA, taking the ionic resistance of these regions into account. The source terms in both anode and cathode catalyst layers correspond to hydrogen oxidation and oxygen reduction reaction at anode and cathode catalyst layers, respectively. The source term in the proton conservation equation is used to describe the transfer current between electrolyte and solid phase inside anode and cathode catalyst layers. The electron transport equation is solved in catalyst layers, diffusion media, and bipolar plates on both cathode and anode sides. Source terms in both anode and cathode catalyst layers correspond to hydrogen oxidation and oxygen reduction reaction, creating or consuming electrons. The transfer current densities are expressed as

$$\text{Anode: } j = ai_o^{ref}\left(\frac{C_{H_2}}{C_{H_2,ref}}\right)^{1/2}\left(\frac{\alpha_a + \alpha_c}{RT}F\eta_a\right) \quad [1]$$

$$\text{Cathode: } j = -ai_o^{ref}\left(\frac{C_{O_2}}{C_{O_2,ref}}\right)\exp\left(-\frac{\alpha_c}{RT}F\eta_c\right) \quad [2]$$

These kinetic expressions represent hydrogen oxidation reaction (HOR) in the anode catalyst layer and oxygen reduction reaction (ORR) in the cathode catalyst layer, respectively. The HOR kinetic expression is a linearized Butler-Volmer equation based on the fact of facile HOR kinetics or small overpotential, whereas the sluggish ORR kinetics causes a large overpotential and the expression for it is obtained by neglecting the anodic reaction term of the Butler-Volmer equation. The value of $(\alpha_a + \alpha_c)$ in HOR kinetics should be equal to 2, while α_c equals 1 in ORR, which corresponds to a Tafel slope of approximately 73 mV/decade at 95°C. Based on the experimental work of Bernardi and Verbrugge[14] and Gottesfield and Zawodzinski,[15] ORR is assumed to be first order kinetics. The surface overpotentials are defined as

$$\text{Anode: } \eta_a = \phi_s - \phi_e \quad [3]$$

$$\text{Cathode: } \eta_c = \phi_s - \phi_e - U_{oc} \quad [4]$$

where U_{oc} is the equilibrium thermodynamic potential and is given by

$$U_{oc} = 1.23 - 9.0 \times 10^{-4}(T - 298.15) \quad [5]$$

The electronic and electrolyte phase potentials, ϕ_s and ϕ_e, are obtained by solving proton and electron transport equations, respectively.

The source terms in the species equations represent the production or consumption of a particular species k in the electrochemical reactions. The equation for water transport contains an extra source term which accounts for electro-osmotic drag of water from the anode to cathode. The mass diffusion coefficient of species k, D_k, in anode and cathode gas channels is calculated as a function of pressure and temperature.[16] For the porous media and catalyst layers, the diffusion coefficient is modified to account for porosity and tortuosity of porous regions, and is given by

$$D_k = D_o\left(\frac{T}{T_o}\right)^{3/2}\left(\frac{P}{P_o}\right) \quad \text{for gas channel}$$

$$D_k = \frac{\varepsilon}{\varsigma}D_o \quad \text{for porous media} \quad [6]$$

where ε and ς are the porosity and tortuosity of the porous media respectively.

The three heat source terms in the energy equations account for the reversible entropic heat, irreversible reaction heat and joule heating in a PEM fuel cell. Readers are referred to Ju et al.[12] for a detailed description of these source terms. In addition, effective heat capacitance is used in porous material given by

$$\rho C_p = \varepsilon(\rho C_p)_f + (1 - \varepsilon)(\rho C_p)_s \quad [7]$$

where the subscript f stands for fluid and s stands for the solid matrix. The transport properties of the electrolyte are given by Springer et al.[17] for Nafion membranes. The proton conductivity, κ_{mem}, electro-osmotic drag coefficient for water, n_d, and the water diffusivity, $D_{w,mem}$, in the membrane are correlated to the water content of the membrane, λ, which is in turn a function of the water activity, a

$$a = \frac{C_w^g RT}{P^{sat}} \quad [8]$$

$$\lambda = \begin{cases} 0.043 + 17.81a - 39.85a^2 + 36.0a^3 & \text{for } 0 < a < 1 \\ 14 + 1.4(a - 1) & \text{for } 1 < a < 3 \end{cases} \quad [9]$$

Table II. Kinetics, physical, and transport properties.

Description	References	Value
Exchange current density x specific reaction surface in anode side, $ai_{0,a}^{\mathrm{ref}}$	Ju et al.[17]	1.0×10^9 A/m^3
Exchange current density x specific reaction surface in cathode side, $ai_{0,c}^{\mathrm{ref}}$	Adjustable	2.0×10^4 A/m^3
Reference hydrogen molar concentration, $C_{\mathrm{H_2,ref}}$	Ju et al.[17]	40.88 mol/m^3
Reference oxygen molar concentration, $C_{\mathrm{O_2,ref}}$	Ju et al.[17]	40.88 mol/m^3
Anodic and cathodic transfer coefficients for hydrogen oxidation reaction		$\alpha_a = \alpha_c = 1$
Cathodic transfer coefficient for oxygen reduction reaction		$\alpha_c = 1$
Dry membrane density, $\rho_{dry,mem}$	Courtesy of Gore	2000 kg/m^3
Equivalent weight of membrane, EW	Courtesy of Gore	1.1 kg/mol
H_2 diffusivity in membrane, $D_{\mathrm{H_2}}^{\mathrm{e}}$	Ju et al.[17]	2.59×10^{-10} m^2/s
O_2 diffusivity in membrane, $D_{\mathrm{O_2}}^{\mathrm{e}}$	Ju et al.[17]	1.22×10^{-10} m^2/s
H_2 diffusivity in the anode gas channel, $D_{0,\mathrm{H_2,a}}$	Bird et al.[15]	1.1028×10^{-4} m^2/s
H_2O diffusivity in the anode gas channel, $D_{0,\mathrm{w,a}}$	Bird et al.[15]	1.1028×10^{-4} m^2/s
O_2 diffusivity in the cathode gas channel, $D_{0,\mathrm{O_2,c}}$	Bird et al.[15]	3.2348×10^{-5} m^2/s
H_2O diffusivity in the cathode gas channel, $D_{0,\mathrm{w,c}}$	Bird et al.[15]	7.35×10^{-5} m^2/s
Thermal conductivity of hydrogen (H_2), $k_{\mathrm{H_2}}$	Bird et al.[15]	0.2040 W/mK
Thermal conductivity of oxygen (O_2), $k_{\mathrm{O_2}}$	Bird et al.[15]	0.0296 W/mK
Thermal conductivity of water vapor, k_w	Bird et al.[15]	0.0237 W/mK
Thermal conductivity of nitrogen (N_2), $k_{\mathrm{N_2}}$	Bird et al.[15]	0.0293 W/mK
Thermal conductivity of membrane, k_{mem}	Courtesy of Gore	0.950 W/mK
Thermal conductivity of macro gas diffusion layer, k_{GDL}	Courtesy of Gore	1.19 W/mK
Thermal conductivity of micro gas diffusion layer, k_{MPL}	Courtesy of Gore	1.19 W/mK
Electronic conductivity of macro gas diffusion layer, σ_{GDL}	Courtesy of Gore	6666.67 S/m
Electronic conductivity of micro gas diffusion layer, σ_{MPL}	Courtesy of Gore	200 S/m
Electronic conductivity of catalyst layer, σ_{cat}	Courtesy of Gore	200 S/m
Electronic conductivity of bipolar plate, σ_{BP}	Courtesy of Gore	20000 S/m

$$\kappa_{mem} = (0.5139\lambda - 0.326)\exp\left[1268\left(\frac{1}{303} - \frac{1}{T}\right)\right] \quad [10]$$

$$n_d = \frac{2.5\lambda}{22} \quad [11]$$

$$D_{w,mem} = \begin{cases} 2.692661843 \times 10^{-10} & for\ \lambda \leqslant 2 \\ 0.87(3-\lambda) + 2.95(\lambda - 2) \times 10^{-10} e^{[7.9782-2416/T]} & for\ 2 < \lambda \leqslant 3 \\ 2.95(4-\lambda) + 1.642454(\lambda - 3) \times 10^{-10} e^{[7.9728-2416/T]} & for\ 3 < \lambda < 4 \\ [2.563 - 0.33\lambda + 0.0264\lambda^2 - 0.00067\lambda^3] \times 10^{-10} e^{[7.9728-2416/T]} & for\ \lambda > 4 \end{cases} \quad [12]$$

The equivalent water concentration in the membrane is defined as

$$C_{w,mem} = \frac{\rho_{dry,mem}\lambda}{EW} \quad [13]$$

The mass diffusivity of species through the membrane is usually much lower than that in gas. In this model, diffusivities of H_2 and O_2 through the membrane are taken to be constant and listed in Table II.

For the present work, Gore-SelectR membrane was chosen. The Gore membrane is a microscopically reinforced composite membrane. The reinforcement provides durability benefits that, in practice, allow thinner membranes, with higher proton conductance and water permeance, to be used. Due to the reinforcement, the proton conductivity and water diffusivity had to be adjusted to approximately half of the value of an unreinforced membrane.[18] Hence it follows that

$$\kappa_{\mathrm{mem}}^{\mathrm{eff}} = \frac{1}{2}\kappa_{\mathrm{mem}} = \frac{1}{2}(0.5139\lambda - 0.326)\exp\left[1268\left(\frac{1}{303} - \frac{1}{T}\right)\right] \quad [14]$$

$$D_{w,mem}^{eff} = \frac{1}{2}D_{w,mem} \quad [15]$$

However, in the anode and cathode catalyst layers Nafion solution is used as ionomer. Consequently, the effective proton conductivity of anode and cathode catalyst layers follows that of the Nafion membrane, with the tortuosity effect. That is

$$\kappa_{\mathrm{cat}}^{\mathrm{eff}} = \frac{\varepsilon_{\mathrm{mc}}}{\varsigma_k}\kappa_{\mathrm{mem}} \quad [16]$$

where $\varepsilon_{\mathrm{mc}}$ is the volume fraction of ionomer in anode and cathode catalyst layers and ς_k is the tortuosity factor for ionomer in catalyst layers. The local current density, I, in the membrane is calculated by

$$I = -\kappa_{\mathrm{mem}}^{\mathrm{eff}}\nabla\phi_e \quad [17]$$

The average current density can be obtained by taking the surface average of local current density over the entire membrane. That is

$$I_{\mathrm{avg}} = \frac{1}{A_{\mathrm{mem}}}\int_{A_{\mathrm{mem}}} IdA \quad [18]$$

Boundary conditions.— A single-domain approach is used to solve the governing equations numerically. Therefore, boundary conditions are required only at the external surfaces of the computational domain. For mass flow, the no-slip and impermeability conditions are applied to all the external surfaces except for the inlets and outlets of anode/cathode gas channels. Inlet species concentrations, $C_{\mathrm{k,in}}$, at the anode and cathode inlets are determined by inlet

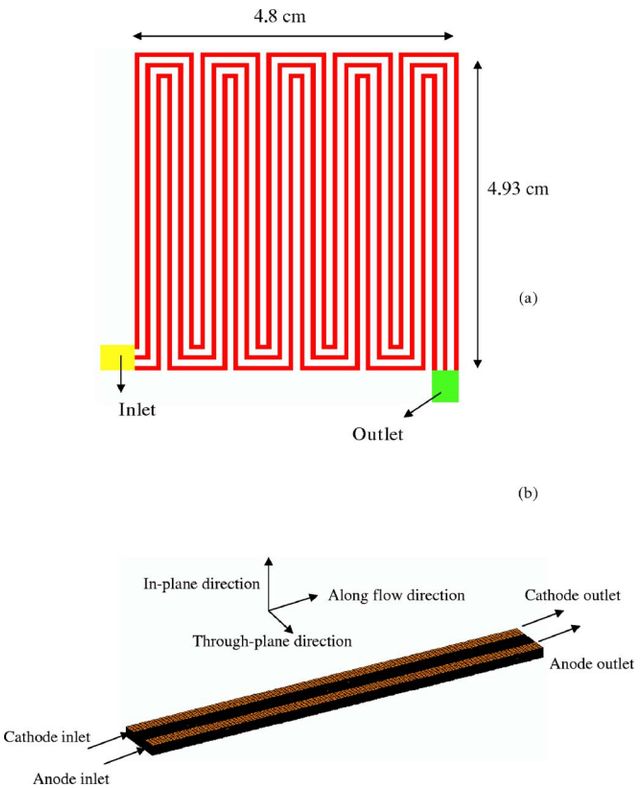

Figure 1. (Color online) (a) Schematic of three-pass serpentine flow-field of 25 cm^2 cell. (b) Schematic of a single-channel cell.

pressures and humidity conditions. Velocities at anode and cathode inlets can be calculated by their respective stoichiometric flow ratios, ξ_a and ξ_c which are defined as the ratio of the amount of reactant supplied to the amount of reactant required by electrochemical reaction to generate the overall current density, I_{avg}

$$V_{a,in} = \xi_a \frac{I_{avg}}{2FC_{H_2,in}} \frac{A_{react}}{A_{a,in}} \quad [19]$$

$$V_{c,in} = \xi_c \frac{I_{avg}}{4FC_{O_2,in}} \frac{A_{react}}{A_{c,in}} \quad [20]$$

At the outlet of the gas channels flow is assumed to be directed outward and otherwise conditions are determined from the upstream. For the present study, constant current density boundary condition is applied at the bipolar plates and cell voltage is iterated until the resulting current density is matched with constant current density specified at bipolar plates. Cell voltage is given by

$$V_{cell} = \phi_{s,c} - \phi_{s,a} \quad [21]$$

where $\phi_{s,a}$ and $\phi_{s,c}$ are electronic phase potential at the anode bipolar plate and cathode bipolar plate, respectively. Constant temperature boundary condition is applied at all the external surfaces of the fuel cell.

Numerical implementation.— The PEM fuel cell model described above is implemented into a commercial computational fluid dynamics (CFD) package, STAR-CD, based on its user coding capability.[19] All of the source terms defined in Table I are specified through user-defined subroutines. In the present work, two numerical meshes are generated. One for the 25 cm^2 experimental cell with three-pass serpentine flow field for the validation study (all the relevant dimensions for the flow field and other subregions are shown in Fig. 1a and Table III). The other is for a single-channel cell to explore the fundamentals of species, heat, and charge transport, as shown in Fig. 1b. Based on the grid independence study of Meng et al.,[20] roughly 2.0 million computational cells are applied to the three-pass serpentine flow-field geometry and roughly 94,000 computational cells to the single-channel geometry. This model requires ~270 s per iteration on an eight-PC cluster (1.4 GHz) for the three-pass serpentine geometry and ~15 s per iteration on a single PC (2 GHz) for the single-channel geometry. The present model requires 1000 iterations to get convergent results.

Results and Discussion

Model validation.— The present PEM fuel cell model was validated against the experimental data of a 25 cm^2 three-pass serpentine flow-field PEM fuel cell operating at 95°C. The predicted cell voltage is compared with the experimental results for two current densities and three different inlet relative humidities (RH). All of the cases and their corresponding results are listed in Table III. The geometric parameters are listed in Table IV. For all the cases, the inlet gas pressure on both anode and cathode was 270 KPa and the anode and cathode stoichiometry ratios were set to 1.3 and 2.0, respectively. In addition, the temperature of all external surfaces was maintained at 95°C, allowing the application of the isothermal boundary condition in the model. A contact resistance of 50 mΩ-cm^2 was applied in all the numerical simulations to account for all the contact resistances within the fuel cell. All properties used in the simulations are listed in Table II. A close agreement between simulated and experimental results, as displayed in Table III, shows that the present model can be used to explore the transport phenomena in a PEM fuel cell operated at elevated temperatures.

Transport phenomena in a single-channel cell.— Higher saturation pressure and hence higher saturated water vapor concentration not only makes membrane hydration more difficult under low-humidity operating conditions, but also decreases oxygen concentration at the inlet of gas channels as compared to 80°C. While high inlet RH at the anode and cathode gas channel provides better humidification to the membrane, it also provides lower inlet oxygen concentration. To fully analyze the effect of inlet RH on cell performance, the same operating conditions as those used for the model validation study were used and summarized in Table III. The oper-

Table III. Model validation results of 25 cm^2 PEM fuel cell for 95 °C operation.

Cases	$\xi_{anode}/\xi_{cathode}$	$RH_{anode}/RH_{cathode}$	Current density (A/cm^2)	Cell voltage (V) (Simulation)	Cell voltage (V) (Experimental)
1	1.3/2.0	50%/50%	0.8	0.700	0.700
2	1.3/2.0	30%/30%	0.8	0.680	0.693
3	1.3/2.0	50%/0%	0.8	0.625	0.637
4	1.3/2.0	50%/50%	1.6	0.525	0.548
5	1.3/2.0	30%/30%	1.6	0.474	0.531
6	1.3/2.0	50%/0%	1.6	0.400	0.437

Table IV. Cell design parameters.

Description	Value	Reference
Anode/cathode macro gas diffusion layer thickness	0.230 mm	Courtesy of Gore
Anode/cathode micro gas diffusion layer thickness	0.060 mm	Courtesy of Gore
Anode/cathode catalyst layer thickness	0.010 mm	Courtesy of Gore
Anode/cathode gas channel depth	0.846 mm	Courtesy of Gore
Anode/cathode bipolar plate thickness	1.59 mm	Courtesy of Gore
Height of cell in the in-plane direction (for 25 cm^2 geometry)	47.695 mm	Courtesy of Gore
Height of cell in the in-plane direction (for single-channel geometry)	1.621 mm	Courtesy of Gore
Membrane width (Gore-SelectR)	0.018 mm	Courtesy of Gore
Porosity of anode/cathode macro gas diffusion layer, ε_{GDL}	0.7	Courtesy of Gore
Porosity of anode/cathode micro gas diffusion layer, ε_{MPL}	0.5	Courtesy of Gore
Porosity of anode/cathode catalyst layer, ε_{cat}	0.6	Courtesy of Gore
Tortuosity of porous layer for species diffusion, ς	1.2	Adjustable
Tortuosity of catalyst layer for ionic conductivity, ς_k	1.25	Adjustable
Volume fraction of ionomer in anode/cathode catalyst layer, $\varepsilon_{\mu c}$	0.26	Courtesy of Gore
Permeability of anode/cathode macro gas diffusion layers, K_{GDL}	4.0×10^{-12} m^2	Courtesy of Gore
Permeability of anode/cathode micro gas diffusion layers, K_{MPL}	2.0×10^{-15} m^2	Courtesy of Gore

ating conditions differ only in the inlet RH, allowing the above-mentioned counter effects of inlet RH to be investigated in detail. For the single-channel unit cell, most of the geometrical dimensions were the same as that of the 25 cm^2 cell, with some different dimensions explicitly mentioned in Table IV. All other input and physical properties used for the study are the same as for the 25 cm^2 cell. To facilitate further discussion, various parametric cases are referred to by their case numbers given in Table III. Various line plots are identified by their inlet RH conditions. For instance, line plot for 50/0 denotes 50% RH at anode inlet and 0% at cathode inlet.

Figure 2 shows the variation of average water activity in the membrane along the flow direction for 0.8 A/cm^2 average current density. Along the flow direction, water activity in the membrane increases due to the water production in the cathode catalyst layer. It is difficult to remove the water from the catalyst layer in the area that is covered by the current collector rib. Therefore, the membrane portion facing the current collector rib (referred to as "rib") has better humidification than the portion facing the gas channel (referred to as "gc"). As seen from the Fig. 2, even at the exit, the membrane is not fully humidified for any case, which shows the difficulty of membrane hydration under 95°C, and low inlet RH operation. Similar variations of water activity are observed for 1.6 A/cm^2 average current density, as shown in Fig. 3. Even at this high current density the membrane is dry, resulting in a large ohmic overpotential.

The average ionic conductivity variations in the membrane portion facing the gas channel and the ribs are shown in Fig. 4 and 5 for 0.8 and 1.6 A/cm^2 average current densities, respectively. The ionic conductivity is dependent on temperature and water content of membrane, which in turn is highly influenced by the operating temperature. An increase in the operating temperature results in significant decrease in the water content of the membrane; hence low ionic conductivity of the membrane. As seen from Fig. 4 and 5, the ionic conductivity of the membrane is below its fully humidified value especially for cases 3 and 6. Even at the exit of the cell the ionic conductivity is very low resulting in large ohmic overpotential.

Current density is governed by the oxygen concentration in the cathode catalyst layer and the ionic conductivity of the membrane. For low humidity operation, there is a strong interplay between oxygen concentration and ionic conductivity. The portion of the MEA

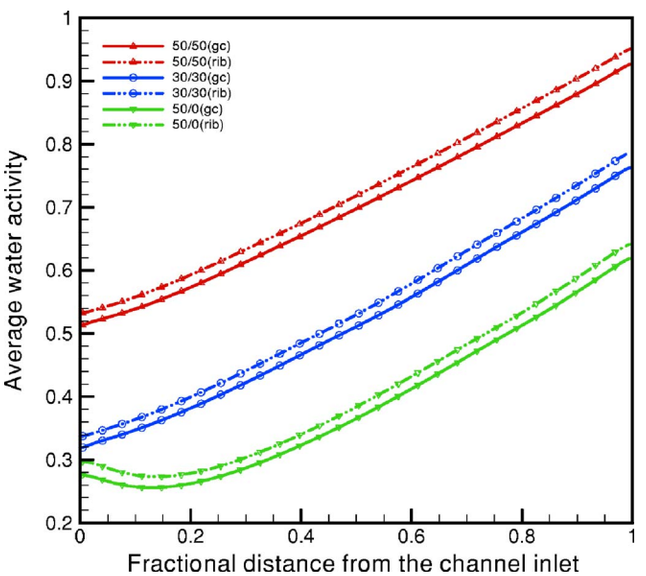

Figure 2. (Color online) Average water activity distribution in different regions of membrane along the flow direction for 0.8 A/cm^2 average current density cases (case 1, 2, and 3).

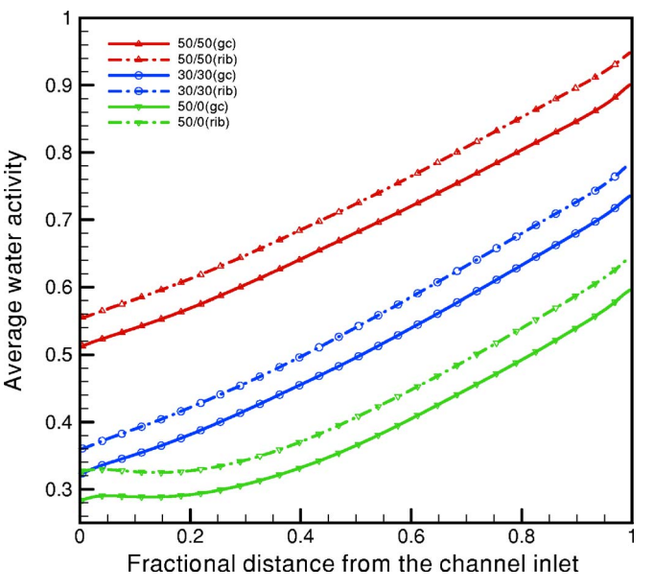

Figure 3. (Color online) Average water activity distribution in different regions of membrane along the flow direction for 1.6 A/cm^2 average current density cases (case 4, 5, and 6).

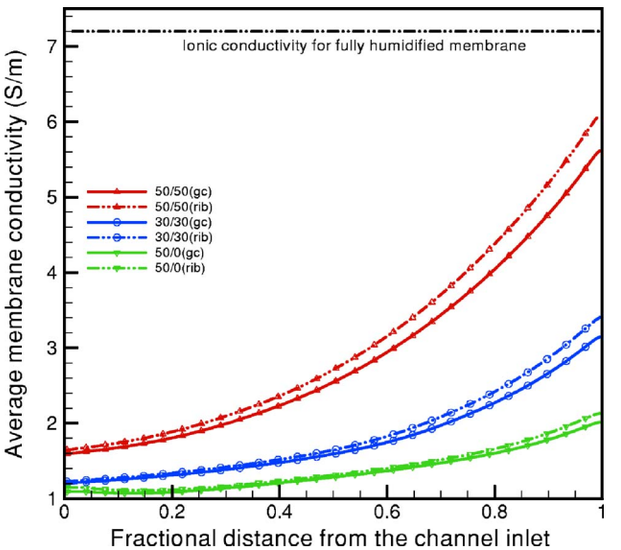

Figure 4. (Color online) Average ionic conductivity distribution in different regions of membrane along the flow direction for 0.8 A/cm^2 average current density cases (case 1, 2, and 3).

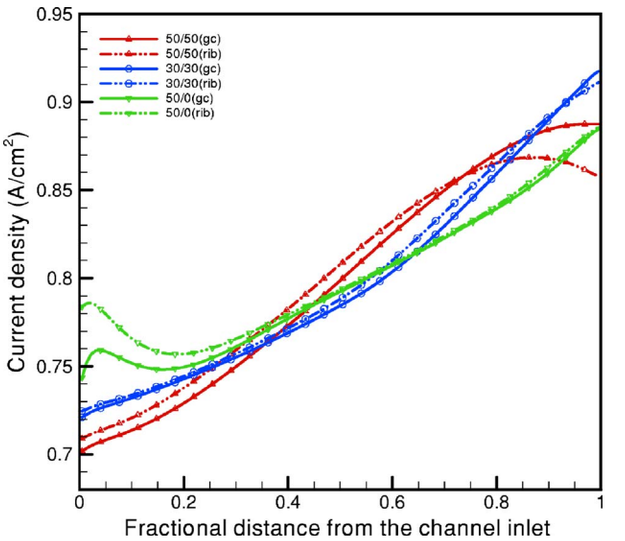

Figure 6. (Color online) Current density distribution in middle section of membrane, facing gas channel and current collector rib, along the flow direction for 0.8 A/cm^2 average current density cases (case 1, 2, and 3).

facing a rib has better ionic conductivity because of the water retention under the rib, whereas the portion of MEA facing a gas channel has higher oxygen concentration. For 95°C operation, the inlet water concentration is higher compared to 80°C operation using the same inlet RH, which in turn reduces the inlet oxygen concentration. Low oxygen concentration in the gas channel results in a smaller driving force for oxygen diffusion through porous layers and thus oxygen transport to the MEA portion facing a rib is more difficult. Figure 6 shows the variation of current density in the middle section of membrane facing the gas channel and the rib. It is seen from Fig. 6 that the lower the inlet humidification level on the cathode side, the higher is the current density at the inlet section. Although low inlet humidity at the cathode gas channel provides poor humidification to the membrane, it also provides higher inlet oxygen concentration. This implies that better availability of oxygen to the active sites dominates over low membrane hydration at the inlet section of a fuel cell operated at 95°C. Along the flow direction, membrane hydration increases at a faster rate than oxygen depletion, causing the current density to increase in this direction. The interplay of oxygen depletion and membrane hydration becomes important toward the outlet of gas channels. For case 1, the current density variation in the membrane region facing the rib shows that the current density is dominated by oxygen depletion towards the outlet. Note that oxygen depletion has become dominant even when the membrane has not become fully humidified. This behavior is in contrast to that of 80°C operation where low inlet RH operations are dominated by membrane hydration but oxygen depletion governs the performance when the membrane becomes fully hydrated.[17] The above-mentioned interplay is even more severe for 1.6 A/cm^2 average current density, as shown in Fig. 7.

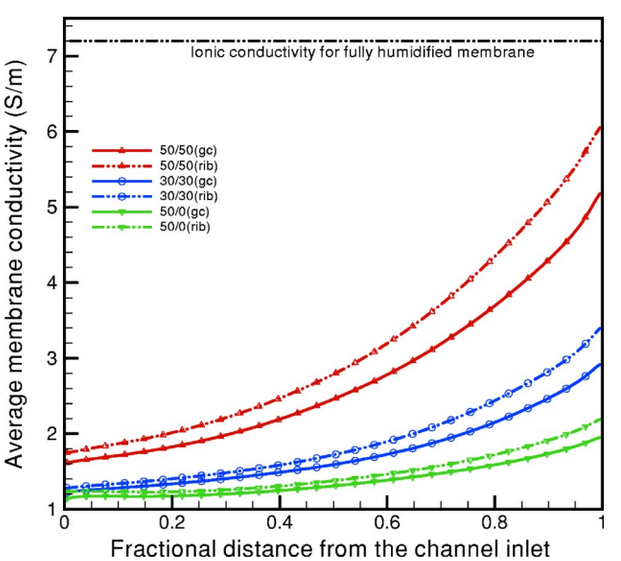

Figure 5. (Color online) Average ionic conductivity distribution in different regions of membrane along the flow direction for 1.6 A/cm^2 average current density cases (case 4, 5, and 6).

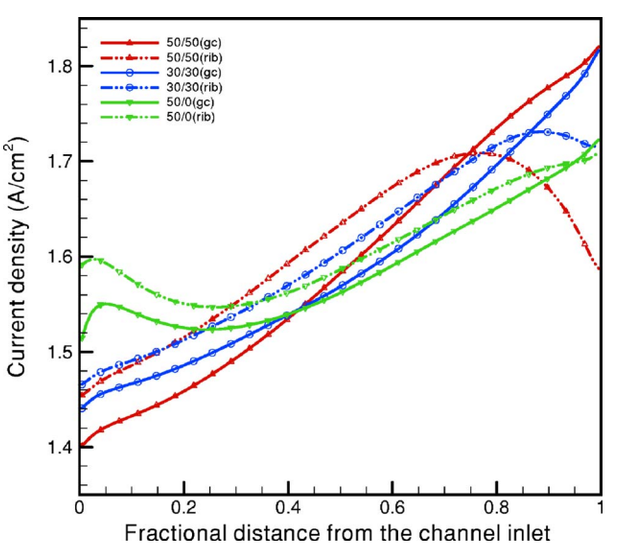

Figure 7. (Color online) Current density distribution in middle section of membrane, facing gas channel and current collector rib, along the flow direction for 1.6 A/cm^2 average current density cases (case 4, 5, and 6).

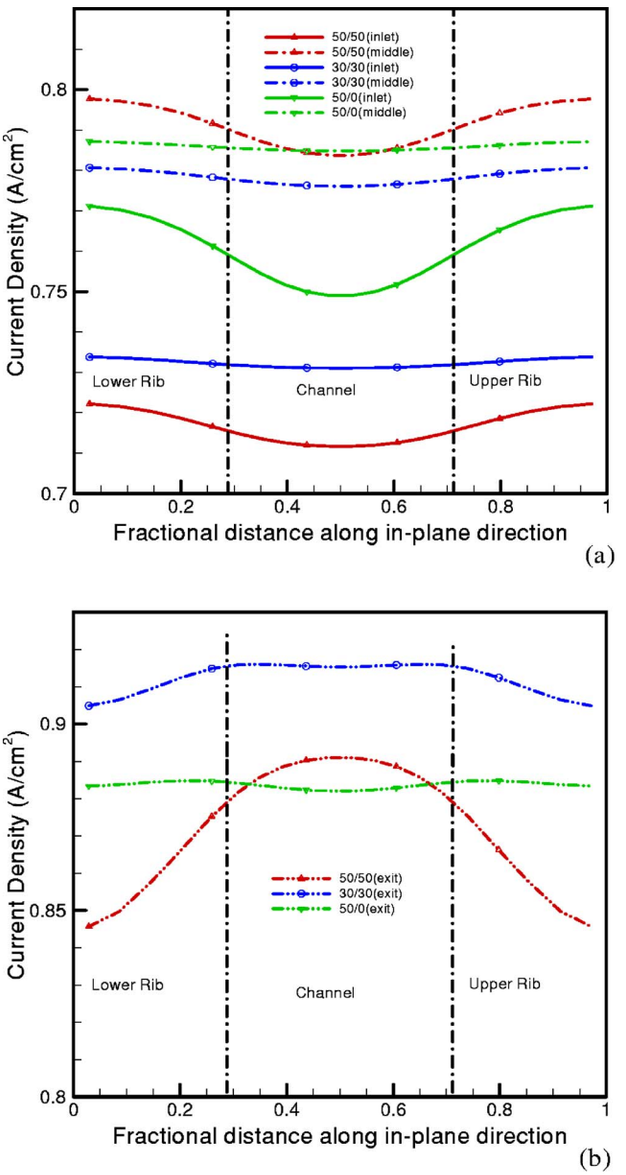

Figure 8. (Color online) Current density distribution in middle section of membrane, along the in-plane direction for 0.8 A/cm^2 average current density cases (case 1, 2, and 3) (a) at the inlet and middle section and (b) at the exit section along the flow direction.

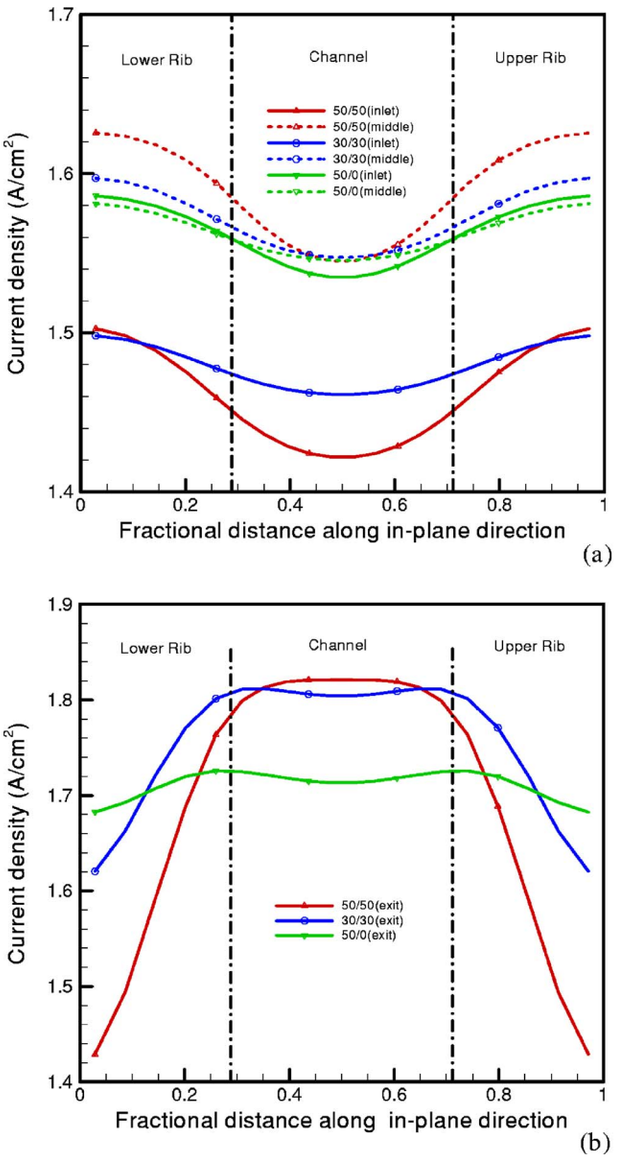

Figure 9. (Color online) Current density distribution in middle section of membrane, along the in-plane direction for 1.6 A/cm^2 average current density cases (case 4, 5, and 6) (a) at the inlet and middle section and (b) at the exit section along the flow direction.

Figure 8 shows the variation of current density in the in-plane direction at different locations along the flow direction for 0.8 A/cm^2 average current density. The interplay of oxygen depletion and membrane hydration is more clearly shown in this figure and the dominant role played by oxygen depletion is confirmed. The inverted bell shape at the inlet section implies that the local current density is governed by membrane hydration, resulting in higher current density for the membrane area facing the rib. The bell shape profile of current density near the exit section shows that current density is governed by availability of oxygen to active sites, providing higher current density to the membrane region facing the gas channel. The bell profile is flatter for cases 2 and 3, showing that the oxygen availability to active site and membrane hydration effects are counterbalancing each other for these cases. Figure 9 shows the current density variation in the in-plane direction for 1.6 A/cm^2 average current density. The current density profiles for cases 5 and 6 near the exit section show that the maximum current density exists at the junction of the gas channel and the rib. The membrane region facing the gas channel suffers from low membrane hydration and the region facing the rib suffers from low oxygen availability in the catalyst layer. The junction of the gas channel and the rib provides the best combination of membrane hydration and oxygen availability; hence the highest current density is obtained there.

Figures 10 and 11 show the temperature increase in the through-plane direction for 0.8 and 1.6 A/cm^2, respectively. The increase in temperature is plotted at the half-cell length cutting across the middle of the flow channel. The temperature peak appears in the cathode catalyst layer, implying that maximum heat generation takes place there. Figures 12 and 13 show the temperature increase in the membrane region under the gas channel and rib along the flow direction for 0.8 and 1.6 A/cm^2, respectively. In all cases, the mem-

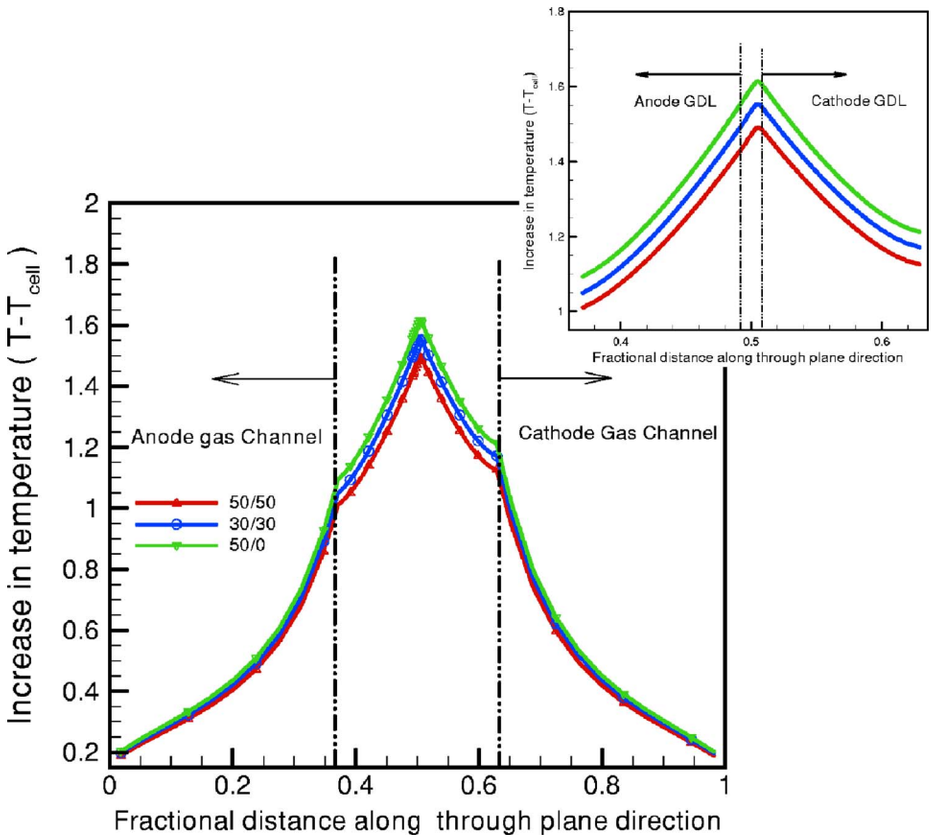

Figure 10. (Color online) Temperature increase in fuel cell under the gas channel in the through-plane direction cut at half-cell length along flow direction for 0.8 A/cm^2 average current density cases (case 1, 2, and 3).

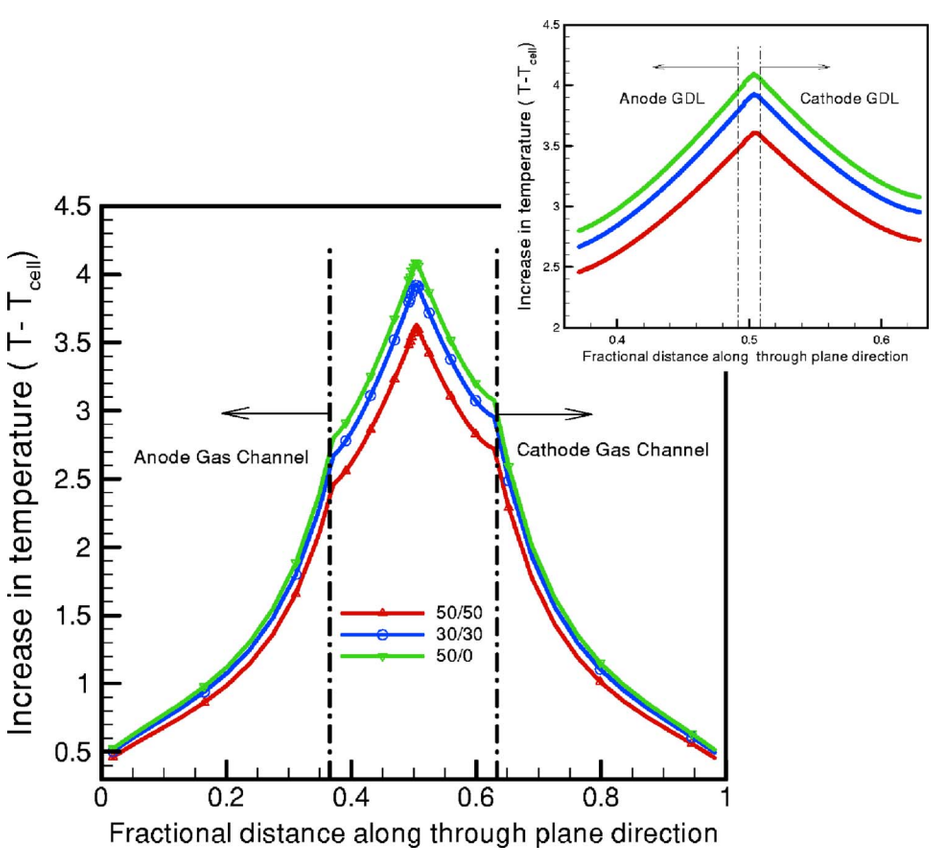

Figure 11. (Color online) Temperature increase in fuel cell under the gas channel in the through-plane direction cut at half-cell length along flow direction for 1.6 A/cm^2 average current density cases (case 4, 5, and 6).

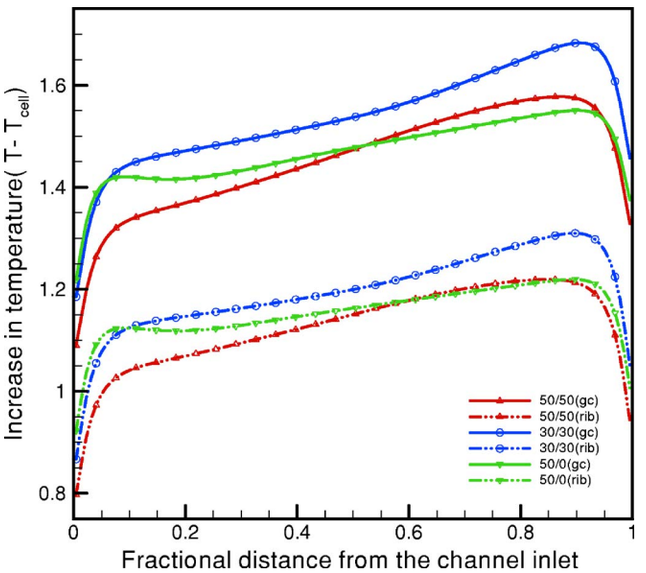

Figure 12. (Color online) Increase in average membrane temperature along the flow direction in different regions of membrane facing gas channel and current collector rib, for 0.8 A/cm^2 average current density cases (case 1, 2, and 3).

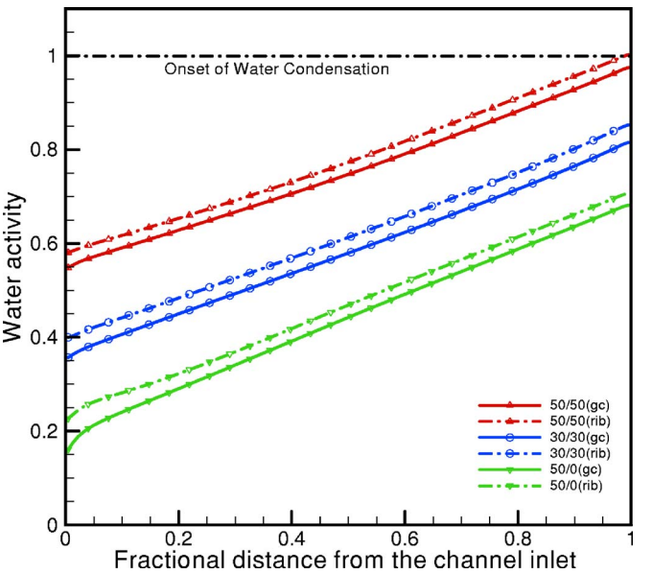

Figure 14. (Color online) Variation of water activity at the interface of cathode catalyst layer and cathode MPL facing the gas channel and rib along the flow direction for 0.8 A/cm^2 average current density cases (cases 1, 2, and 3).

brane temperature facing the gas channel is higher than that facing the current collector rib because the rib acts as heat sink due to their high thermal conductivity.

The onset of vapor condensation can be predicted by water activity. Water activity greater than unity means the presence of liquid water, though the single-phase model will treat it as supersaturated vapor. Figures 14 and 15 show the variation of water activity at the interface of cathode catalyst layer and micro porous layer (MPL), along the flow direction. As shown from Fig. 14 and 15, water vapor condenses in the cathode catalyst layer portion under the ribs, towards the channel exit for 50/50 case (50% inlet relative humidity at both anode and cathode gas channels). However, the average membrane proton conductivity is below the fully humidified value as shown in Fig. 4 and 5. This indicates that low membrane hydration is a result of membrane drying on the anode side.

Effect of flow-field design on cell performance.— Two flow-field designs are commonly used in practice: the serpentine flow field and the parallel flow field. The parallel flow field incurs less pressure drop between outlet and inlet of gas channels in comparison to the serpentine flow field. Parallel flow field also provides more uniform distribution of reactant over the whole active area. A main disadvantage of the parallel flow field design, however,

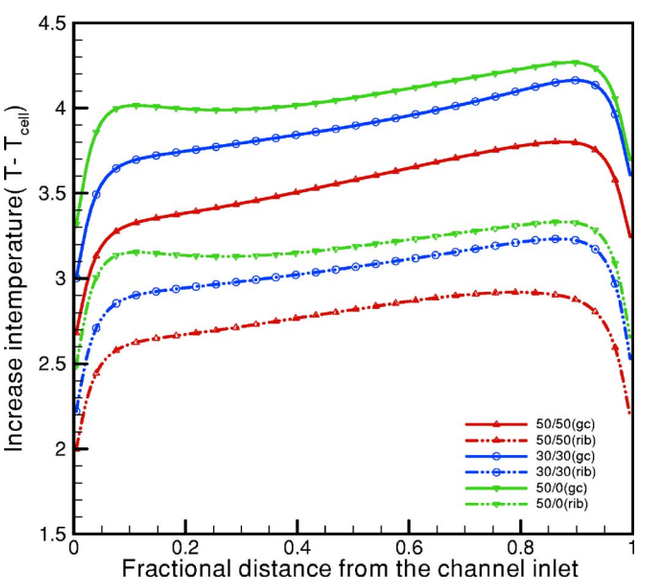

Figure 13. (Color online) Increase in average membrane temperature along the flow direction in different regions of membrane facing gas channel and current collector rib, for 1.6 A/cm^2 average current density cases (case 4, 5, and 6).

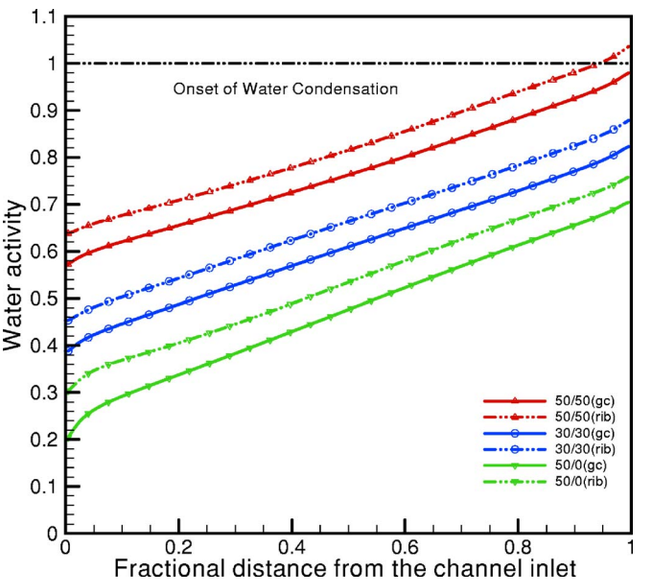

Figure 15. (Color online) Variation of water activity at the interface of cathode catalyst layer and cathode MPL facing the gas channel and rib along the flow direction for 1.6 A/cm^2 average current density cases (cases 4, 5, and 6).

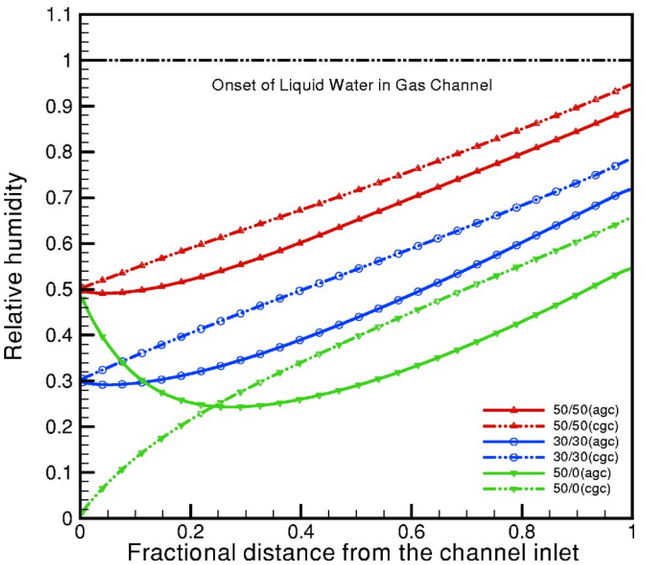

Figure 16. (Color online) Variation of relative humidity in middle section of gas channel of a 25 cm^2 cell with parallel flow-field design, along the flow direction for 0.8 A/cm^2 average current density cases (cases 1, 2, and 3).

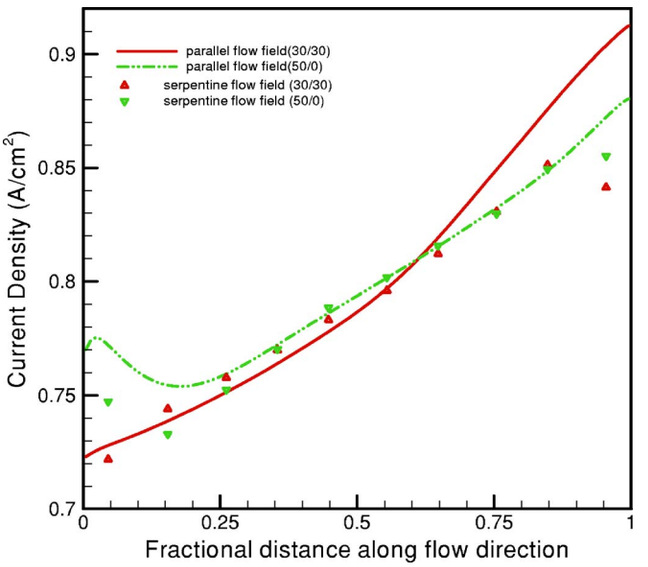

Figure 18. Variation of current density along the flow direction for 25 cm^2 fuel cell having serpentine and parallel flow-field design at average current density of 0.8 A/cm^2 average current density.

is clogging of the gas channel by liquid water. Once a channel becomes clogged, the active area under it becomes inactive for the rest of the operation, whereas the serpentine flow field can flush out liquid water more easily via high gas flow rate and bypassing of the gas through the GDL is possible as well.

The parallel flow-field design is periodic in its structure and the performance under any gas channel is not influenced by other channels. Thus, a PEM fuel cell with parallel flow field is numerically equivalent to a single-channel cell having the same dimensions in the through plane and along the flow direction with a periodic extension in the in-plane direction. Figures 16 and 17 represent the variation of RH in the gas channels for a 25 cm^2 parallel flow-field fuel cell for 95°C operation. As seen from these figures, the RH is less than unity, even at the channel exits for all cases. This indicates that liquid water cannot appear in gas channels and no channel clogging is possible. This feature makes the parallel flow field a viable option uniquely suited for 95°C operation. Figure 18 shows the current density variation, averaged over the gas channel and rib portion, along the flow direction in the middle section of membrane for the serpentine flow field and parallel flow field with 25 cm^2 active area for 0.8 A/cm^2 average current density and two different inlet RH conditions (30/30 and 50/0 cases). All other parameters are the same for the two fuel cells. As shown in Fig. 18, the local current density towards the gas channel exit is governed by oxygen depletion for the serpentine flow field, whereas it is governed by membrane hydration for the parallel flow field. The current density distribution confirms that oxygen depletion is more critical towards the gas channel exit for the serpentine flow-field design. A detailed study of effects of serpentine vs parallel flow field on cell performance will be presented in a separate publication.

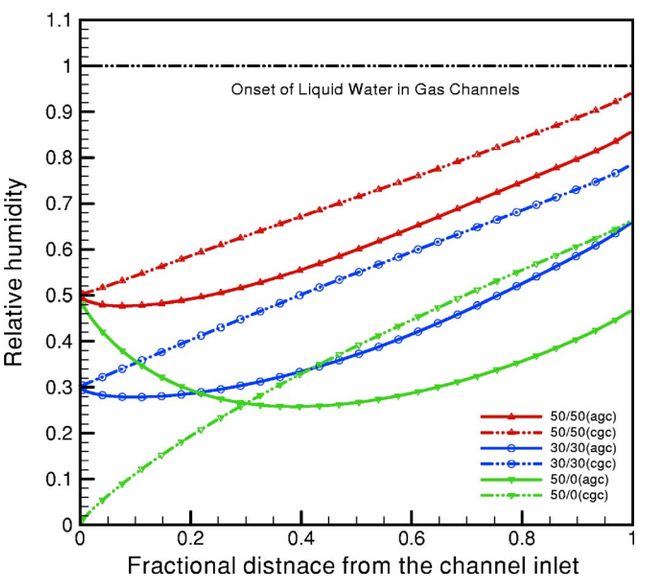

Figure 17. (Color online) Variation of relative humidity in middle section of gas channel of a 25 cm^2 cell with parallel flow-field design, along the flow direction for 1.6 A/cm^2 average current density cases (cases 4, 5, and 6).

Conclusions

A three-dimensional, single-phase, nonisothermal model was applied to study transport phenomena in a PEM fuel cell operated at elevated temperatures. Better ORR kinetics, low membrane hydration, and a dominant oxygen depletion effect were identified as the main characteristics of cell operation at 95°C. The effects of these characteristics were investigated under various operating conditions. The results show that the inlet humidity strongly affects cell performance. Oxygen depletion along the flow direction dominates membrane hydration toward the exit of a fuel cell, especially at high current densities. Thus, both oxygen depletion and membrane hydration should be taken into consideration while determining the optimum inlet RH, especially for high current density operations. Dry operation of fuel cells for 95°C operation makes parallel flow field an attractive alternative to serpentine flow field and results in more uniform current density.

Acknowledgment

Funding for this work from W. L. Gore & Associates, Inc. is gratefully acknowledged.

The Pennsylvania State University assisted in meeting the publication costs of this article.

List of Symbols

a	water activity
A	area, m^2
c	molar concentration, mol/m^3
cgc	cathode gas channel
D	mass diffusivity of species, m^2/s
EW	equivalent molecular weight of electrolyte in membrane, kg/mol
F	Faraday constant, 96487 C/mole
I	current density, A/m^2
j	transfer current, A/m^3
k	thermal conductivity, W/mK
K	hydraulic permeability, m^2
p	pressure, Pa
n	number of electrons in electrochemical reaction
n_d	electro-osmotic drag coefficient
R	the universal gas constant, 8.314 J/mol·K
RH	relative humidity
s	stoichiometry coefficient in electrochemical reaction
S	source term in transport equation
T	temperature, K
$\boldsymbol{u}$	velocity vector, m/s
V_{cell}	cell potential, V
U_{oc}	thermodynamic equilibrium potential, V

Greek

α	transfer coefficient
ε	volume fraction of gaseous phase in porous region
ε_{mc}	volume fraction of ionomer phase in catalyst layer
ϕ	phase potential, V
η	overpotential, V
κ	ionic conductivity, S/m
λ	membrane water content, mol H_2O/mol SO_3^-
μ	fluid viscosity, kg/ms
ρ	density, kg ‖ m^3
$\rho_{dry,mem}$	dry membrane density, kg ‖ m^3
τ	viscous stress, N/m^2
ξ	stoichiometry flow ratio

Subscripts

a	anode
avg	average value
c	cathode
cat	catalyst
e	electrolyte
g	gas phase
GDL	gas diffusion layer
H_2	hydrogen
i	regions index
in	channel inlet
mem	membrane
k	species index
O_2	oxygen
react	electrochemical reaction
ref	reference value
s	electronic
sat	saturation value
T	energy equation
u	momentum equation
w	water
Φ	potential equation
0	standard condition, 298.15 K and 101.3 kPa (1 atm)

Superscripts

e	electrolyte
eff	effective value in porous region
mem	membrane
g	gas
ref	reference value
sat	saturation value

References

1. S. Rogg, M. Hoglinger, E. Zwittig, C. Pfender, W. Kaiser, and T. Heckenberger, *Fuell Cells*, **3**, 153 (2003).
2. R. K. A. M. Mallant, *J. Power Sources*, **118**, 424 (2003).
3. S. J. Lee, S. Mukerjee, E. A. Ticianelli, and J. McBreen, *Electrochim. Acta*, **44**, 3283 (1999).
4. M. Murthy, M. Esayian, W.-k. Lee, and J. W. Van Zee, *J. Electrochem. Soc.*, **150**, A29 (2003).
5. S. Malhotra and R. Datta, *J. Electrochem. Soc.*, **144**, L23 (1997).
6. C. Yang, P. Costamanga, S. Srinivasan, J. Benziger, and A. B. Bocarsly, *J. Power Sources*, **103**, 1 (2001).
7. V. Ramani, H. R. Kunz, and J. M. Fenton, *J. Membr. Sci.*, **232**, 31 (2004).
8. V. Ramani, H. R. Kunz, and J. M. Fenton, *Electrochim. Acta*, **50**, 1181 (2005).
9. K. T. Adjemian, S. J. Lee, S. Srinivasan, J. Benziger, and A. B. Bocarsly, *J. Electrochem. Soc.*, **149**, A256 (2002).
10. M. F. Mathias, R. Makharia, H. A. Gasteiger, J. J. Conley, T. J. Fuller, C. J. Gittleman, S. S. Kocha, D. P. Miller, C. K. Mittelsteadt, T. Xie, S. G. Yan, and P. T. Yu, *Electrochem. Soc. Interface*, **14**, 24 (2005).
11. S. Um, C. Y. Wang, and K. S. Chen, *J. Electrochem. Soc.*, **147**, 4485 (2000).
12. H. Meng and C. Y. Wang, *J. Electrochem. Soc.*, **151**, A 358 (2004).
13. H. Ju, H. Meng, and C. Y. Wang, *Int. J. Heat Mass Transfer*, **48**, 1303 (2005).
14. D. M. Bernardi and M. W. Verbrugge, *AIChE J.*, **37**, 1151 (1991).
15. S. Gottesfeld and T. A. Zawodzinski, *Advances in Electrochemical Science and Engineering*, Vol. 5, C. Tobias, Editor, p. 195, John Wiley & Sons, New York (1997).
16. R. B. Bird, W. E. Stewart, and E. N. Lightfoot, *Transport Phenomena*, John Wiley & Sons, New York (2002).
17. T. E. Springer, T. A. Zawodizinski, and S. Gottesfeld, *J. Electrochem. Soc.*, **136**, 2334 (1991).
18. H. Ju, C. Y. Wang, S. Cleghorn, and U. Beuscher, *J. Electrochem. Soc.*, **152**, A1645 (2005).
19. STAR-CD Version 3.15 Methodology, CD-Adapco Group (2001).
20. H. Meng and C. Y. Wang, *Chem. Eng. Sci.*, **59**, A3331 (2004).